Micro- and nano-porosity of the active Alpine Fault zone, New Zealand

Martina Kirilova[1], Virginia Toy[1,2], Katrina Sauer[1], François Renard[3,4], Klaus Gessner[5,6], Richard Wirth[7], Xianghui Xiao[8,9], and Risa Matsumura[2]

[1]Institut für Geowissenschafte, Johannes Gutenberg Universität-Mainz, J. J. Becher Weg 21D-55128, Mainz, Germany

[2]Department of Geology, University of Otago, PO Box 56, Dunedin 9054, New Zealand

[3]Department of Geosciences, The Njord Centre, University of Oslo, Oslo 0316, Norway.

[4]Université Grenoble Alpes, Université Savoie Mont Blanc, CNRS, IRD, IFSTTAR, ISTerre, BP53, 38041 Grenoble, France.

[5]Geological Survey of Western Australia, 100 Plain Street, East Perth, WA 6004, Australia.

[6]School of Earth Sciences, The University of Western Australia, 35 Stirling Highway, Crawley, WA 6009

[7]Helmholtz-Zentrum Potsdam, GFZ, Sektion 4.3, Telegrafenberg, 14473 Potsdam, Germany

[8]Advanced Photon Source, Argonne National Laboratory, Lemont, IL 60439, USA

[9]National Synchrotron Light Source II, Brookhaven National Laboratory, Upton, NY 11973, USA

Correspondence to: Martina Kirilova (martina.kirilova@uni-mainz.de)

Abstract

Porosity reduction in rocks from a fault core can cause elevated pore fluid pressures, and consequently influence the recurrence time of earthquakes. We investigated the porosity distribution in the New Zealand's Alpine Fault core in samples recovered during the first phase of the Deep Fault Drilling Project (DFDP-1B) by using two-dimensional nanoscale and three-dimensional microscale imaging. Synchrotron X-ray microtomography-derived analyses of open pore spaces show total microscale porosities in the range of 0.1-0.24%. These pores have mainly non-spherical, elongated, flat shapes and show subtle bipolar orientation. Scanning and transmission electron microscopy reveal the samples' microstructural organization, where nanoscale pores ornament grain boundaries of the gouge material, especially clay minerals. Our data imply that: (i) the porosity of the fault core is very small and not connected, (ii) the distribution of clay minerals controls the shape and orientation of the associated pores; (iii) porosity was reduced due to pressure solution processes; and (iv) mineral precipitation in fluid-filled pores can affect the mechanical behaviour of the Alpine Fault by decreasing the already critically low total porosity of the fault core, causing elevated pore fluid pressures, and/or introducing weak mineral phases, and thus lowering the overall fault frictional strength. We conclude that the current state of very low porosity in the Alpine Fault core is likely to play a key role in the initiation of the next fault rupture.

1. Introduction

Fault mechanics, fault structure and fluid flow properties of damaged fault rocks are intimately related (e.g. Gratier and Gueydan, 2007; Faulkner et al., 2010). Fault rupture is associated with intense brittle fracturing that enhances porosity, and thus permeability, and therefore also possible rates and directions of fluid propagation within fault zones (e.g. Girault et al., 2018). Conversely, post seismic recovery mechanisms (gouge compaction and pressure

37 solution processes) result in reductions of porosity, permeability and fluid flow (Renard et al, 2000; Faulkner et al.,
38 2010; Sutherland et al., 2012). These processes may cause elevated pore fluid pressures within fault cores, and
39 trigger frictional failure (e.g. Sibson, 1990; Gratier et al., 2003; Zhu et al., 2020). Therefore, the state of porosity
40 within rocks from fault cores can play a key role in fault slip.

41 The Alpine Fault of New Zealand is late in its seismic cycle (Cochran et al., 2017), so studying it allows us to
42 investigate pre-earthquake conditions that may influence earthquake nucleation and rupture processes. Recently,
43 drilling operations were undertaken in this fault zone to investigate the *in situ* conditions (Sutherland et al, 2012,
44 2017). Slug tests in the DFDP-1B borehole (Sutherland et al., 2012) and laboratory permeability measurements of
45 core samples (Carpenter et al., 2014) indicate permeability decreases by six orders of magnitude with increasing
46 proximity to the fault. Furthermore, Sutherland et al. (2012) documented a 0.53 MPa fluid pressure difference across
47 the principal slip zone (PSZ) of the fault, which suggests that the fault core has significantly lower permeability than
48 the surrounding cataclasite units. It is therefore interpreted to act as a fault seal that limits fluid circulation within its
49 hanging wall (Sutherland et al., 2012). Permeability variations like this are closely associated with the porosity
50 evolution of fault cores, and thus are likely to affect the fault strength and seismic properties (Sibson, 1990; Renard
51 et al., 2000; Gratier and Gueydan, 2007).

52 In this study, we investigate the porosity distribution in rocks from the Alpine Fault core and consider the potential
53 effects of this porosity on fault strength. We have measured open pore spaces in these rocks from X-ray computed
54 tomography (XCT) datasets and examined pore morphology by implementing quantitative shape analyses.
55 Lithological and microstructural characteristics of these samples were performed by using scanning electron
56 microscopy (SEM) and transmission electron microscopy (TEM).

57 ## 2. Geological setting

58 New Zealand`s Alpine Fault (Fig. 1a) is a major active crustal-scale structure that ruptures in a large earthquake
59 every 291 ± 23 years, the last one of which occurred in 1717 (Cochran et al., 2017). The fault is the main constituent
60 of the oblique transform boundary between the Australian Plate and the Pacific Plate, accommodating around 75%
61 of the relative plate motion. Ongoing dextral strike-slip at 27 ± 5 mm yr^{-1} along the fault has resulted in a total
62 strike-separation of ~ 480 km over the last 25 Ma (Norris and Cooper, 1995, 2001; Norris and Toy, 2014). In
63 Neogene time, a dip-slip component added to the fault motion has resulted in more than 20 km of vertical uplift of
64 the hanging wall (Norris and Cooper, 1995, 2001; Norris and Toy, 2014). Consequently, rocks comprising the
65 hanging wall of the fault have been exposed in various outcrops, where they can be studied in detail. The
66 amphibolite facies Alpine Schist is the metamorphic protolith of a ~ 1 km thick mylonite zone, which has been
67 exhumed from depth and now structurally overlies an up to 50 m thick zone of brittlely deformed cataclasites and
68 gouges (e.g. Norris and Cooper, 1995, 2001; Norris and Toy, 2014). These rocks have been investigated in outcrops
69 and from samples collected in three boreholes during the two phases of the Deep Fault Drilling Project (DFDP-1A,
70 DFDP-1B and DFDP-2B; Fig. 1a) along the Alpine Fault (Sutherland et al., 2012; Toy et al., 2015; Toy et al., 2017).

71 Most of the brittle shear displacement along the fault has been accommodated within the fault core, which includes
72 Principal Slip Zone (PSZ) gouges and cataclasite-series rocks (Toy et al., 2015). Both in surface outcrops and drill
73 core samples, the Alpine Fault manifests as a thin (5 to 20 cm thick) gouge zone with a predominantly random fabric
74 of clay-rich material (Toy et al., 2015; Schuck et al., 2020). This cohesive but uncemented layer has a grain size
75 significantly finer than the surrounding cataclasite units, which shows that the material was reworked only within
76 this layer, most probably as a result of ultra-comminution due to multiple shear events under brittle conditions
77 (Boulton et al., 2012; Toy et al., 2015). The local presence of authigenic smectite clays (Schleicher et al., 2015) and
78 calcite and/or chlorite mineralization within sealed fractures and in the gouge matrix (Williams et al, 2017) indicate
79 that mineral reactions are restricted to an alteration zone within the fault core (Sutherland et al., 2012; Schuck et al.,
80 2020). The Alpine Fault core has been interpreted to have formed during a cyclical history of mineralization, shear,
81 and fragmentation (Toy et al., 2015). In addition, in the DFDP-1B borehole (Fig. 1b, Sutherland et al., 2012) fault

82 gouges occur at two distinct depths: 128.1 m (PSZ-1) and 143.85 m (PSZ-2), which shows that the slip was not
83 localized within a single gouge layer (Toy et al., 2015).

3. Sample description and analytical methods

3.1 Samples

86 Porosity analyses were performed on four samples representing PSZ gouges and cataclasites of the Alpine Fault
87 core, which were recovered from the DFDP-1B borehole (Fig. 1b, c; Sutherland et al., 2012). These are DFDP-1B
88 58_1.9, DFDP-1B 69_2.48, DFDP-1B 69_2.54 and DFDP-1B 69_2.57. Sample nomenclature includes drill core run
89 number, section number, and centimeters measured from the top of each section. These samples were recovered
90 from drilled depth of 126.94 m, 143.82 m, 143.88 m and 143.91 m, respectively.

91 Detailed lithological and microstructural descriptions of the DFDP-1B drill core were carried out simultaneously
92 with, and after the drilling operations by the DFDP-1 Science Team, and these data were later summarized by Toy et
93 al. (2015). Samples DFDP-1B 58_1.9 and DFDP-1B 69_2.48 belong to foliated cataclasite units (Fig. 1b, c; Toy et
94 al., 2015), described as ultracataclasites with gouge-filled shear zones located above PSZ-1 and PSZ-2 respectively.
95 Sample DFDP-1B 69_2.54 represents the gouge layer that defines PSZ-2, whereas sample DFDP-1B 69_2.57 is
96 composed of brown ultracataclasites that belong to the lower cataclasite unit (Fig. 1b, c; Toy et al., 2015).

3.2 X-ray computed tomography (XCT)

98   We imaged the samples using X-ray absorption tomography, where the signal intensity depends on how electron
99   density and bulk density attenuate a monochromatic X-ray along its path through the material (e.g. Fusseis et al.
100 2014). We acquired the X-ray microtomography data for this study at the 2-BM beamline of the Advanced Photon
101 Source, Argonne National Laboratories USA in December 2012. The non-cylindrical samples of ~7 mm height and
102 ~ 4 mm diameter were mostly drilled parallel to the foliation, mounted on a rotary stage, and imaged with a beam
103 energy of 22.5 keV. A charge-couple device camera collected images at 0.25° rotation steps over 180°. A sample-
104 detector distance of 70 mm yielded a field-of-view of 2.81 mm. The voxel size (i.e. spatial sampling) was 1.3 µm
105 and the spatial resolution ranged from two to three times the voxel size. We have reconstructed the datasets with a
106 filtered back-projection parallel beam reconstruction into 32-bit gray level volumes consisting of 2048 * 2048 *
107 2048 voxels using X-TRACT (Gureyev et al., 2011).

3.3 Analyses of XCT datasets

109 Data analyses and image processing were performed using the commercial software Avizo 9.1™ (Fig. 2). Initially,
110 the datasets were rescaled to 8-bit grey scale volumes for enhanced computer performance. In addition, small
111 volumes of interest were cropped from the whole volume before a non-local means filter was applied to reduce noise
112 (Buades et al., 2005). For each voxel, this filter compares the value of this voxel with all neighboring voxels in a
113 given search window. A similarity between the neighbors determines a correction applied to each voxel (e.g.
114 Thomson et al., 2018).

115 On the filtered gray-scale images, pores were identified as disconnected materials of the darkest grey-scale range
116 (Fig. 2a, Supplementary material 1: Fig. 1). The corresponding gray-scale values were thresholded, and the datasets
117 were converted into binary form. This step is called segmentation. Several segmentation techniques exist, from
118 thresholding at a given gray scale value (e.g. Ianossov et al., 2009; Andrew et al., 2013) to deep learning algorithms
119 (Ma et al., 2020). It is up to the user to choose the segmentation technique that is most appropriate to analyze a given
120 dataset. To our knowledge, no single segmentation technique can be generalized and universally used independently
121 of the nature of the samples. In the present study, we have chosen a simple segmentation technique by applying a
122 threshold to the gray scale images to separate the void space from the solid. This technique has been used in many
123 studies in the last two decades to characterize porosity in rocks, including some very recent studies in rock physics
124 (Macente et al., 2019; Renard et al., 2019). The segmented porosity volume depends strongly on the choice of the

125 threshold and some studies have demonstrated that the final porosity estimated by different segmentation methods
126 can vary by 20% (Andrä et al., 2013). However, when the level of noise in the data is low, the differences in
127 porosities estimated by different segmentation techniques is negligible (Andrew, 2018). Our data were acquired at a
128 synchrotron where the parallel beam and high photon flux ensured a low level of the noise in the images. In
129 addition, application of a non-local-means filter applied to our data reduced the noise level. For these reasons, we
130 consider that it was robust to apply a simple thresholding technique to this dataset but acknowledge that the porosity
131 values we estimate could differ by <20% from the 'true' porosity of the rock (cf. Andrä et al., 2013; Hapca et al.,
132 2013).

133 However, our segmentation procedure also captured cracks within a sample, which are likely to result from
134 depressurization during core recovery (Fig. 2b, Supplementary material 1: Fig. 1). To omit the cracks, we utilized
135 the morphological operation 'connected components' available in the software Avizo 9.1, which allows volumes
136 larger than selected number of connected voxels to be excluded from the binary label images. To each sample we
137 applied upper limits of 20 ($43.94 \mu m^3$), 50 ($109.85 \mu m^3$), 100 ($219.7 \mu m^3$) and 200 ($439.4 \mu m^3$) face connected
138 voxels. Total porosities estimates based on these operations are presented as percentages of the sample volume in
139 Supplementary material 1: Table 1. Unfortunately, this methodology results in either loss of larger pores or inclusion
140 of small cracks depending on the implemented limit of connected components, and thus the calculated porosities
141 include significant bias. Therefore, the operation 'connected components' was used only for visualization purposes,
142 and clusters of 200 face connected voxels were created to show the 3D volumes of segmented pore spaces (Fig. 2c)

143 Instead, the volumes and shape characteristics of segmented materials (including cracks i.e. without any data
144 limitation) were exported from Avizo software in numerical format, and volume distributions within a sample were
145 plotted on a logarithmic scale (Fig. 3). Data up to a specific volume size were fit to a polynomial curve, and then the
146 curve was extrapolated to the X-axis intercept, which is the expected maximum pore size (Fig. 3). For each sample
147 the total porosity was then estimated by integrating the curve, which excludes all volumes on the right side of the
148 curve. Total porosities are presented as a percentage of the whole sample volume (Fig. 3). The implemented
149 equations are given in Supplementary material 1.

150 Pore shapes were analyzed on bivariate histograms plotted by using the numerical pore characteristics, previously
151 extracted from Avizo software. Only pore volumes between $21.97 \mu m^3$ (10 voxels) and $878.8 \mu m^3$ (400 voxels) were
152 included to avoid bias in the data due to insufficient voxel count and presence of cracks, respectively. Individual
153 pores in our dataset are separated (Fig. 2c).The covariance matrix of each pore was calculated, and the three
154 eigenvalues of this covariance matrix were extracted. These three values correspond to the three main orthogonal
155 directions in each pore (i.e. the longest, medium and shortest axes) and we use them as proxies to describe pore
156 geometry. Thus, their amplitudes provide information on the spatial extension of a given pore and its shape. The
157 ratio between the medium and largest eigenvalues of each pore defines its elongation (Fig. 4), the ratio between the
158 smallest and the largest eigenvalues defines its sphericity (Fig. 5), and the ratio of the smallest and the medium
159 eigenvalues defines its flatness (Fig. 6).

160 The angles θ and φ that describe the orientation of the longest eigenvalue (i.e. axis) of each pore with respect to the
161 global orthogonal axes system of the 3D scan were calculated. These angles were translated into trend and plunge
162 and then plotted on a lower hemisphere equal area stereographic projection with a probability density contour to
163 display the distribution of pore unit orientations (Fig. 7).

164 **3.4 Scanning electron microscopy (SEM)**

165 SEM images were collected on Zeiss Sigma-FF-SEM at the University of Otago's Centre for Electron Microscopy.
166 The SEM was operated at a working distance of 8.5 mm, a**n accelerating** voltage of 10 keV and a 120 μm aperture
167 with dwell time of 100μs. EDS maps were created by using Aztec Software (https://www.oxford-
168 instruments.com/products/microanalysis/energy-dispersive-x-ray-systems-eds-edx/eds-for-sem/eds-software-aztec).

169 **3.5 Transmission electron microscopy (TEM)**

170 TEM images were collected on a FEI Tecnai G2 F20 X-Twin transmission electron microscope, located at the
171 German Research Centre for Geosciences (GFZ), Potsdam, Germany (Fig. 9). The instrument is equipped with field-
172 emission gun (FEG) electron source and high-angle annular dark-field (HAADF) Detector. Images were collected
173 from samples placed on a Gatan double-tilt holder at an accelerating voltage of 200kV. These TEM samples were
174 prepared by focused ion beam (FIB) milling at GFZ Potsdam using a HELIOS system operated at an accelerating
175 voltage of 30 kV.

4   Results

4.1 XCT-derived characteristics of porosity

178 All samples contain low total porosities, ranging from 0.1% to 0.24% (Fig. 3). If different segmentation techniques
179 were applied, a variability in the range that Andrew (2018) demonstrated is reasonable, from nearly 0% to 20%,
180 would correspond to porosities between 0.08% and 0.29% in our samples. It can be noted that the lower cataclasite
181 sample (DFDP-1B 69_2.57) has twice as much pore space (Fig. 3d) as any of the other samples. The characterized
182 pore volume distributions range over almost three orders of magnitude for all samples (Fig. 3). Furthermore, the
183 expected maximum pore volume was estimated to be largest in the PSZ-2 sample (DFDP-1B 69_2.54), reaching 862
184 μm^3 (Fig. 3c).

185 In all samples, shape analyses of pores with volumes between 21.97 μm^3 (10 voxels) and 878.8 μm^3 (400 voxels)
186 demonstrate predominantly elongated (Fig. 4), non-spherical (Fig. 5) and flat pore shapes (Fig. 6). This is
187 particularly pronounced for the smaller pore volumes. The number of elongated pores per sample increases in the
188 upper foliated cataclasites (Fig. 4a and b) with increasing proximity to PSZ-2, where most elongated pores occur
189 (Fig. 4c). Conversely, the lower cataclasite sample demonstrates proportionally fewer elongated pores within the
190 sample (Fig. 4d). The degree of sphericity is uniform for all samples, and pores appear as mainly non-spherical (Fig.
191 5). Few isolated spherical pores are manifested only by small pore volumes (Fig. 5). A trend of increasing the
192 number of flat pores is observed with increasing sample depth (Fig. 6), and most flat pores are detected in the lower
193 cataclasite (Fig. 6d).

194 The orientations of the individual pore units show two distinctive peaks with opposite vergence, defining bipolar
195 distributions of pore orientations (Fig. 7). The observed bipolarity is subtle in samples DFDP-1B 58_1.9 (Fig. 7a)
196 and DFDP-1B 69_2.48 (Fig. 7b), and more obvious in samples DFDP-1B 69_2.54 (Fig. 7c) and DFDP-1B 69_2.57
197 (Fig. 7d).

4.2 Microstructural characteristics of porosity

199 To demonstrate the microstructural arrangement of the cataclasites, we show representative SEM images from
200 sample DFDP-1B 69_248 (Fig. 8), previously described as a 'lower foliated cataclasite' by Toy et al., 2015. SEM
201 images presented here reveal rounded to sub-rounded crystalline clasts up to 100 µm in diameter (Fig. 8a, b), which
202 consist of ~50 % plagioclase, ~40 % K-feldspar, and ~10 % quartz and are elongated at angles of 0-30° to the
203 foliation. The surrounding matrix material is composed of finer grains (< 30 µm in diameter) of white micas,
204 chlorite, K-feldspar, calcite and Ti-oxide (Fig. 8c). Numerous quartz clasts contain microfractures, filled by calcite
205 and/or chlorite.

206 TEM characterization of the gouge material from PSZ-2 (sample DFDP-1B 69_2.54) reveals that the Alpine Fault
207 gouges are composed of angular quartz and/or feldspar fragments (~200 nm in size), wrapped by smaller
208 phyllosilicates (< 100 nm long). This random fabric is ornamented by nanoscale pores (< 50 nm), distributed along
209 all grain and phase boundaries, but especially abundant within/around clay minerals (Fig. 9a).

210 The gouge material also demonstrates phyllosilicate-rich areas, defined by an increase in the clay/clast ratio. In these
211 zones, fine (< 100 nm long) and coarser (few µm long) clay grains coexist and are aligned in wavy fabric that

212 surrounds sporadic protolith fragments (Fig. 9b). Pore spaces are again distributed along the boundaries of the
213 constituent mineral grains but some of them are larger (~0.5 µm) with thin ellipsoidal or elongated shapes (Fig. 9b,
214 c). These pores are commonly associated with inter-clay layer porosity. Large size pores are also observed along
215 quartz-feldspar phase boundaries. These latter pores are associated with multiple grains and occasionally disrupt the
216 boundaries, thus were labelled as fracture porosity (Fig. 9d).

217 **5   Discussion**

218 **5.1 Characteristics of porosity within the Alpine Fault core**

219 Porosity analyses of samples from, or in close proximity to the two PSZs encountered in the DFDP-1B drill core
220 reveal total pore volumes between 0.1% and 0.24% (Fig. 3). These values are significantly lower than the porosity
221 estimates from other active faults in the world, such as: 0.2 to 5.7% total porosity in the core of the Nojima Fault,
222 Japan (Surma et al., 2003) and 0 to 18% in the San Andreas Fault core (Blackburn et al., 2009). The Alpine Fault
223 core contains total pore space volumes comparable only with the lower porosities in these previous studies. It should
224 be noted that the smallest pore spaces captured in the XCT datasets are 1.3 µm in size due to acquisition constraints,
225 whereas nanoscale porosity was identified on the TEM images. Therefore, the estimated total porosities from XCT
226 data represent only minimum values of the open pore spaces in the Alpine Fault core.

227 TEM images presented here mainly focus on nano-scale materials (Fig. 9a, c, d) but were also used to describe the
228 distribution of micro-porosity in these rocks (Figure 9b). The pores visible on grain and phase boundaries in figure
229 9b have similar sizes to the pores segmented on XCT images (> 1.3 µm in diameter), thus we conclude that this is
230 the typical habit of both nano- and micro-pores within the Alpine Fault core (Fig. 9). In addition, both quantitative
231 micro-porosity shape analyses (Fig. 4, 5 and 6) and nano-pores identified on TEM images (Fig. 9) reveal that a
232 significant population of pores are predominantly non-spherical with elongated, flat shapes. We attribute this
233 observation to the tendency of these pores to ornament clay minerals where pores are distributed and elongated
234 along their (001) planes (Fig. 9b, c and d).

235 Foliation in the upper cataclasites is defined by clay-sized phyllosilicates, that become more abundant with
236 proximity to the PSZ (Toy et al., 2015), where a weak clay fabric is developed (Schleicher et al., 2015). This gradual
237 enrichment in clay minerals coincides with the subtle development of bipolar distributions of pore orientations with
238 increasing sample depth (Fig. 7). This observation and the fact that pores are mainly distributed along grain
239 boundaries of clays (Fig. 9) suggest that the distribution of clay minerals also controls pore orientations within the
240 Alpine Fault core. Previously, the phyllosilicate foliation in the Alpine Fault cataclasites has been used to define
241 shear direction (Toy et al., 2015). Thus, we speculate that pore orientations in these rocks are also systematically
242 related to the kinematic framework of the shear zone. If these pores represent remnants of fluid channels, their
243 spatial orientation is likely to reflect the fluid flow directions during deformation. To address this possibility more
244 data for systematic analyses of pore orientations are needed.

245 **5.2 Porosity reduction within the Alpine Fault core**

246 The comparatively lower porosity estimates of the Alpine Fault core than other active faults (e.g. the Nojima Fault,
247 Surma et al., 2003, and the San Andreas Fault, Blackburn et al., 2009) could be attributed to the fact that the Alpine
248 Fault is late in its c. 300 year seismic cycle and the last seismic event occurred in 1717 (Cochran et al., 2017). Thus,
249 we propose that the fault has almost completely sealed. Porosity of fault cores is believed to evolve during the
250 seismic cycle, since fault rupture can cause porosities to increase up to 10% (Marone et al., 1990), and subsequent
251 healing mechanisms (such as mechanical compaction of the fault gouge and/or elimination of pore spaces within the
252 fault core due to pressure solution processes) cause porosity to decrease over time (Sibson, 1990; Renard et al.,
253 2000; Faulkner et al., 2010). SEM data presented here show that fine-grained chlorite and muscovite grains formed
254 as a cement in the cataclastic matrix (Fig. 8c). Our TEM data reveal the abundance of newly precipitated authigenic
255 clays, wrapped around coarser clay minerals (Fig. 9b). Furthermore, delicate clay minerals form fringe structures

256 (Fig. 9a), and strain shadows (Fig. 9c) around larger quartz-feldspar grains. These microstructural observations
257 demonstrate that pressure solution processes operated within these rocks (Toy et al., 2015).

258 Evidence for pressure solution processes has been previously documented in all units, comprising the Alpine Fault
259 core (Toy et al., 2015). Abundant precipitation of alteration minerals (Sutherland et al., 2012), calcite filled
260 intragranular and cross-cutting veins (Williams et al., 2017), and the occurrence of newly formed smectite clays
261 (Schleicher et al., 2015) indicate extensive fluid-rock reactions. In addition, anastomosing networks of opaque
262 minerals (such as graphite; Kirilova et al., 2017), which define foliation in the upper cataclasites (Toy et al., 2015),
263 have been interpreted to be concentrated by pressure solution processes during aseismic creep (Toy et al., 2015;
264 Gratier et al., 2011). The petrological characteristics of the Alpine Fault core lithologies indicate that solution
265 transfer was likely the dominant mechanism for pore closure within these rocks.

266 Porosity estimates presented here are so low that presumably negligible variations in between samples can represent
267 significant gradients in porosity. For example, the increase of total porosity in sample DFDP-1B 69-2.57 with only
268 0.14%, manifests as twice as many open pore spaces in comparison to the rest of the analyzed samples (Fig. 3). In
269 addition, this is the only footwall sample analyzed here and as already mentioned in section 3.1 does not contain any
270 gouge material. Post-rupture porosity reduction is known to operate three to four times faster within fine-grained
271 fault gouges than in coarser-grained cataclasites (Walder and Nur, 1984; Sleep and Blanpied, 1992; Renard et al.,
272 2000) which may explain the porosity differences demonstrated above. Furthermore, previous studies documented
273 less carbonate and phyllosilicate filling of cracks in the Alpine Fault footwall cataclasites than in the hanging wall
274 cataclasites (Sutherland et al., 2012; Toy et al., 2015), suggesting more reactive fluids are present and isolated
275 within the hanging wall of the Alpine Fault. Thus, more intense dissolution-precipitation processes took place in the
276 fault`s hanging wall, which very likely resulted in more efficient porosity reduction, as demonstrated by our porosity
277 estimates (Fig. 3).

278 **5.3 Effects of porosity on the Alpine Fault strength**

279 Very low porosity estimates are presented here (Fig. 3). Very low permeabilities of 10^{-18} m^2 were also measured
280 experimentally in clay-rich cataclasites and gouges from the Alpine Fault zone (Carpenter et al., 2014). In addition,
281 the documented difference of total porosities between the hanging wall and footwall samples (Fig. 3) may be
282 interpreted to reflect different intensities of pressure solution processes, and thus compartmentalization of
283 percolating fluids. Our porosity data show a spatial trend similar to the permeability measurements of Carpenter et
284 al. (2014). This observation yields increased confidence in the interpretation of Carpenter et al. (2014) of a
285 permeability gradient with distance from the PSZ, which itself acts as a hydraulic seal (Sutherland, et al., 2012). The
286 existence of such a barrier to flow is characteristic for faults undergoing creep and locked faults (Rice, 1992;
287 Labaume et al., 1997; Wiersberg and Erzinger, 2008). However, much higher permeabilities in the surrounding
288 damaged rocks (Carpenter et al., 2014) allow fast propagation of fluids within them and can cause localization of
289 high fluid pressures on one side or the other of a hydraulic seal (Sibson, 1990). Such fluid pressures can enhance
290 gouge compaction and pressure solution processes, which will eventually introduce zones of weakness and thus may
291 trigger fault slip (Faulkner et al., 2010).

292 Previous studies and the observations presented here show that fluids were present in the Alpine Fault rocks. Fluid-
293 filled pores represent a favorable environment for mineral precipitation, which can affect the fault strength in two
294 ways: (i) Very small decrease of these critically low total porosities due to mineral precipitation would cause fluid
295 pressurization, which is a well-known fault weakening mechanism described by Byerlee (1990) and Sibson (1990);
296 however, this pressure increase could be slightly offset by inclusion of fluids into new hydrous minerals; (ii)
297 deposition of frictionally weak phases (such as clay minerals and graphite), especially if they decorate grain contacts
298 and/or form interlinked weak layers, would lower the overall frictional strength (Rutter et al., 1976; Niemeijer et al.,
299 2010).

300   Precipitated authigenic clay minerals were identified in our TEM data (Fig. 9) and also documented by previous
301   studies (Schleicher et al., 2015). As well as having low frictional strengths (Moore and Lockner, 2004), clay
302   minerals may also contribute to the formation of an impermeable seal if they form an aligned fabric, which can
303   enhance the likelihood of fluid-pressurization in the fault rocks (Rice, 1992; Faulkner et al., 2010). In addition,
304   graphite, which was previously documented in these rocks (Kirilova et. al., 2017), may effectively weaken the fault
305   due to mechanical smearing (Rutter et al., 2013) and/or localized precipitation within strained areas (Upton and
306   Craw, 2008). Such graphite precipitation within shear surfaces was previously documented by Kirilova et al. (2017).

307   In summary, the presence of trapped fluids in the low porosity rocks of the Alpine Fault core possibly controls the
308   mechanical behavior of the fault and could be responsible for future rupture initiation due to fluid pressurization
309   and/or precipitation of weak mineral phases. This hypothesis is further supported by an experimental study showing
310   that the DFDP-1 gouges are frictionally strong in the absence of elevated fluid pressure (Boulton et al., 2014).

311   6   Conclusions

312   Analyses of XCT-datasets and TEM images of borehole samples from the core of the Alpine Fault reveal micro- and
313   nanoscale pores, distributed along grain boundaries of the constituent mineral phases, especially clay minerals. The
314   tendency of these pores to ornament clays defines their predominantly non-spherical, elongated, flat shapes and the
315   bipolar distribution of pore orientations. The documented extremely low total porosities (in the range 0.1-0.24 %) in
316   these rocks suggest effective porosity reduction and fault healing. Microstructural observations presented here and
317   documented in previous studies indicate that pressure solution processes were the dominant healing mechanism, and
318   that fluids were present in these rocks. Therefore, fluid-filled pores may be places where elevated pore fluid
319   pressures develop, due to further mineral precipitation that decreases the already critically low total porosities.
320   Alternatively, these pores may also facilitate the deposition of weak mineral phases (such as clay minerals and
321   graphite) that may very effectively weaken the fault. We conclude that the current state of the fault core porosity is
322   possibly a controlling factor on the mechanical behaviour of the Alpine Fault and will likely play a key role in the
323   initiation of the next fault rupture.

324   Data availability.

325   Avizo screenshots, total porosity estimates, Matlab script and numerical data of pore volumes can be found in
326   Supplementary material 1.

327   Authors contribution

328   Kirilova reconstructed, processed, and analysed the XCT datasets presented here, interpreted the TEM data and
329   prepared the manuscript. Most of this work was performed during Kirilova's PhD under the academic guidance of
330   Toy. Toy and Gessner collected the XCT data with technical support by Xiao. Renard and Sauer contributed with
331   valuable discussion about XCT data analyses and edited the manuscript. Wirth enabled TEM data acquisition and
332   provided his expertise on TEM data interpretation. Matsumura collected and analyzed the presented SEM data. The
333   final version of this manuscript benefits from collective intellectual input.

334   Competing interests

335   The authors declare that they have no conflict of interest.

References

349 Andrä, H., Combaret, N., Dvorkin, J., Glatt, E., Han, J., Kabel, M., Keehmd, Y., Krzikallac, F., Leed, M.,
350 Madonnae, C., Marshb, M., Mukerjic, T., Saengere, E. H., Sainf, R., Saxenac, N., Rickera, S., Wiegmanna, A., and
351 Zhanf, X.: Digital rock physics benchmarks—Part I: Imaging and segmentation, Computers & Geosciences, 50, 25-
352 32, 2013.

353 Andrew, M.: A quantified study of segmentation techniques on synthetic geological XRM and FIB-SEM images,
354 Computational Geosciences, 22(6), 1503-1512, 2018.

355 Berryman, K. R., Cochran, U. A., Clark, K. J., Biasi, G. P., Langridge, R. M., and Villamor, P.: Major earthquakes
356 occur regularly on an isolated plate boundary fault, Science, 336(6089), 1690-1693, 2012.

357 Blackburn, E. D., Hadizadeh, J., and Babaie, H. A.: A microstructural study of SAFOD gouge from actively
358 creeping San Andreas Fault zone: Implications for shear localization models, *in* AGU Fall Meeting Abstracts, 2009.

359 Buades, A., Coll, B. and Morel, J. M.: A non-local algorithm for image denoising, *in* Computer Vision and Pattern
360 Recognition, IEEE Computer Society Conference, Vol. 2, pp. 60-65, 2005.

361 Boulton, C., Carpenter, B. M., Toy, V., and Marone, C.: Physical properties of surface outcrop cataclastic fault
362 rocks, Alpine Fault, New Zealand, Geochemistry, Geophysics, Geosystems, 13, Q01018,
363 doi:10.1029/2011GC003872, 2012.

364 Boulton, C., Moore, D. E., Lockner, D. A., Toy, V. G., Townend, J., and Sutherland, R.: Frictional properties of
365 exhumed fault gouges in DFDP-1 cores, Alpine Fault, New Zealand, Geophysical Research Letters, 41(2), 356-362,
366 2014.

367 Byerlee, J.: Friction, overpressure and fault normal compression, Geophysical Research Letters, 17(12), 2109-2112,
368 1990.

369 Carpenter, B. M., Kitajima, H., Sutherland, R., Townend, J., Toy, V. G., and Saffer, D. M.: Hydraulic and acoustic
370 properties of the active Alpine Fault, New Zealand: Laboratory measurements on DFDP-1 drill core, Earth and
371 Planetary Science Letters, 390, 45-51, 2014.

372 Cochran, U. A., Clark, K. J., Howarth, J. D., Biasi, G. P., Langridge, R. M., Villamor, P., Berryman, K. R., and
373 Vandergoes, M. J.: A plate boundary earthquake record from a wetland adjacent to the Alpine fault in New Zealand
374 refines hazard estimates, Earth and Planetary Science Letters, 464, 175-188, 2017.

375 Faulkner, D. R., Jackson, C. A. L., Lunn, R. J., Schlische, R. W., Shipton, Z. K., Wibberley, C. A. J., and Withjack,
376 M. O.: A review of recent developments concerning the structure, mechanics and fluid flow properties of fault
377 zones, Journal of Structural Geology, 32(11), 1557-1575, 2010.

378   Fusseis, F., Xiao, X., Schrank, C., and De Carlo, F.: A brief guide to synchrotron radiation-based microtomography
379   in (structural) geology and rock mechanics, Journal of Structural Geology, 65, 1-16, 2014.

380   Girault, F., Adhikari, L. B., France-Lanord, C., Agrinier, P., Koirala, B. P., Bhattarai, M., and Perrier, F.: Persistent
381   CO_2 emissions and hydrothermal unrest following the 2015 earthquake in Nepal, Nature Communications, 9(1),
382   2956, 2018.

383   Gratier, J.-P., Favreau, P., and Renard, F.: Modelling fluid transfer along California faults when integrating pressure
384   solution crack sealing and compaction processes, Journal of Geophysical Research, 108, 2104,
385   doi:10.1029/2001JB000380, B2, 2003.

386   Gratier, J. P.: Fault permeability and strength evolution related to fracturing and healing episodic processes (years to
387   millennia): the role of pressure solution, Oil and Gas Science and Technology–Revue d'IFP Energies nouvelles,
388   66(3), 491-506, 2011.

389   Gratier, J. P., and Gueydan, F.: Effect of Fracturing and Fluid–Rock Interaction on Seismic Cycles, Tectonic Faults:
390   Agents of Change on a Dynamic Earth, 95, 319e356, 2007.

391   Gureyev, T.E., Nesterets, Y., Ternovski, D., Wilkins, S.W., Stevenson, A.W., Sakellariou, A. and Taylor, J.A. :
392   Toolbox for advanced x-ray image processing, in Advances in Computational Methods for X-Ray Optics II edited
393   by M Sanchez del Rio and O Chubar, Advances in Computational Methods for X-Ray Optics II, San Diego, USA,
394   21-25 August 2011: SPIE - The International Society of Optics and Photonics 8141, 2011.

395   Iassonov, P., Gebrenegus, T., and Tuller, M.: Segmentation of X-ray computed tomography images of porous
396   materials: A crucial step for characterization and quantitative analysis of pore structures. Water resources research,
397   45(9), W09415, doi:10.1029/2009WR008087, 2009.

398   Janssen, C., Wirth, R., Reinicke, A., Rybacki, E., Naumann, R., Wenk, H. R., and Dresen, G.: Nanoscale porosity in
399   SAFOD core samples (San Andreas Fault), Earth and Planetary Science Letters, 301(1), 179-189, 2011.

400   Hapca, S. M., Houston, A. N., Otten, W., and Baveye, P. C.: New local thresholding method for soil images by
401   minimizing grayscale intra-class variance, Vadose Zone Journal, 12(3), 12 (3): vzj2012.0172, 2013.

402   Labaume, P., Maltman, A. J., Bolton, A., Tessier, D., Ogawa, Y., and Takizawa, S.: Scaly fabrics in sheared clays
403   from the décollement zone of the Barbados accretionary prism, in Shipley, T.H., Ogawa, Y., Blum, P., and Bahr,
404   J.M. (Eds.), Proceedings of the Ocean Drilling Program Scientific Results, 59-78, 1997.

405   Kirilova, M., Toy, V. G., Timms, N., Halfpenny, A., Menzies, C., Craw, D., Beyssac, O., Sutherland, R., Townend,
406   J., Boulton, C., Carpenter, B., Cooper, A., Grieve, J., Little, T., Morales, L., Morgan, C., Mori, H., Sauer, K.,
407   Schleicher, A., Williams, J., and Craw, L.: Textural changes of graphitic carbon by tectonic and hydrothermal
408   processes in an active plate boundary fault zone, Alpine Fault, New Zealand, Geological Society, London, Special
409   Publications, 453, SP453-13, 2017.

410   Ma, X., Kittikunakorn, N., Sorman, B., Xi, H., Chen, A., Marsh, M., Mongeau, A., Piché, N., WilliamsIII, E. O.,
411   and Skomski, D.: Application of Deep Learning Convolutional Neural Networks for Internal Tablet Defect
412   Detection: High Accuracy, Throughput, and Adaptability, Journal of Pharmaceutical Sciences, 109(4), 1447-1457,
413   2020.

414   Macente, A., Vanorio, T., Miller, K. J., Fusseis, F., and Butler, I. B.: Dynamic Evolution of Permeability in
415   Response to Chemo-Mechanical Compaction, Journal of Geophysical Research: Solid Earth, 124(11), 11204-11217,
416   2019.

417 Marone, C., Raleigh, C. B., and Scholz, C. H.: Frictional behavior and constitutive modeling of simulated fault
418 gouge, Journal of Geophysical Research: Solid Earth, 95(B5), 7007-7025, 1990.

419 Niemeijer, A., Marone, C., and Elsworth, D.: Fabric induced weakness of tectonic faults, Geophysical Research
420 Letters, 37, L03304, doi:10.1029/2009GL041689, 2010.

421 Norris, R. J., and Cooper, A. F.: Origin of small-scale segmentation and transpressional thrusting along the Alpine
422 fault, New Zealand. Geological Society of America Bulletin, 107(2), 231-240, 1995.

423 Norris, R. J., and Cooper, A. F.: Late Quaternary slip rates and slip partitioning on the Alpine Fault, New Zealand.
424 Journal of Structural Geology, 23(2), 507-520, 2001.

425 Norris, R. J., and Toy, V. G.: Continental transforms: A view from the Alpine Fault, Journal of Structural Geology,
426 64, 3-31, 2014.

427 Renard, F., Gratier, J. P., and Jamtveit, B.: Kinetics of crack-sealing, intergranular pressure solution, and
428 compaction around active faults, Journal of Structural Geology, 22(10), 1395-1407, 2000.

429 Renard, F., McBeck, J., Cordonnier, B., Zheng, X., Kandula, N., Sanchez, J. R., Kobchenko, M., Noiriel, C., Zhu,
430 W., Meakin, P., Fusseis, F., and Dag K. Dysthe: Dynamic in situ three-dimensional imaging and digital volume
431 correlation analysis to quantify strain localization and fracture coalescence in sandstone, Pure and Applied
432 Geophysics, 176(3), 1083-1115, 2019.

433 Rice, J. R.: Fault stress states, pore pressure distributions, and the weakness of the San Andreas fault, International
434 Geophysics, 51, 475-503, 1992.

435 Rutter, E. H., and Elliott, D.: The kinetics of rock deformation by pressure solution, Philosophical Transactions for
436 the Royal Society of London, Series A, Mathematical and Physical Sciences, 283, 203-219, 1976.

437 Rutter, E. H., Hackston, A. J., Yeatman, E., Brodie, K. H., Mecklenburgh, J., and May, S. E.: Reduction of friction
438 on geological faults by weak-phase smearing, Journal of Structural Geology, 51, 52-60, 2013.

439 Schleicher, A. M., Sutherland, R., Townend, J., Toy, V. G., and Van Der Pluijm, B. A.: Clay mineral formation and
440 fabric development in the DFDP-1B borehole, central Alpine Fault, New Zealand, New Zealand Journal of Geology
441 and Geophysics, 58(1), 13-21, 2015.

442 Schuck, B., Schleicher, A. M., Janssen, C., Toy, V. G., and Dresen, G.: Fault zone architecture of a large plate-
443 bounding strike-slip fault: a case study from the Alpine Fault, New Zealand. Solid Earth, 11(1), 95-124, 2020.

444 Sibson, R. H.: Conditions for fault-valve behaviour, Geological Society, London, Special Publications, 54(1), 15-28,
445 1990.

446 Sleep, N. H., and Blanpied, M. L.: Creep, compaction and the weak rheology of major faults, Nature, 359(6397),
447 687-692, 1992.

448 Surma, F., Géraud, Y., and Pezard, P.: Porosity network of the Nojima fault zone in the Hirabayashi hole (Japan), *in*
449 EGS-AGU-EUG Joint Assembly, 2003.

450 Sutherland, R., Eberhart-Phillips, D., Harris, R. A., Stern, T., Beavan, J., Ellis, S Henrys, S., Cox, S., Norris, R.J.,
451 Berryman, K.R. and Townend, J.: Do great earthquakes occur on the Alpine fault in central South Island, New
452 Zealand?, In: A continental plate boundary: tectonics at South Island, New Zealand, Geophysical Monograph,
453 American Geophysical Union, 235-251, 2007.

454   Sutherland, R., Toy, V. G., Townend, J., Cox, S. C., Eccles, J. D., Faulkner, D. R Prior, D.J., Norris, R.J., Mariani,
455   E., Boulton, C. and Carpenter, B.M.: Drilling reveals fluid control on architecture and rupture of the Alpine fault,
456   New Zealand, Geology, 40(12), 1143-1146, 2012.

457   Sutherland, R., Townend, J., Toy, V., Upton, P., Coussens, J., Allen, M., and Boles, A.: Extreme hydrothermal
458   conditions at an active plate-bounding fault, Nature, 546, 137-140, doi: 10.1038/nature22355, 2017.

459   Toy, V. G., Boulton, C. J., Sutherland, R., Townend, J., Norris, R. J., Little, T. A., and Scott, H.: Fault rock
460   lithologies and architecture of the central Alpine fault, New Zealand, revealed by DFDP-1 drilling, Lithosphere,
461   L395-1, 2015.

462   Toy, V. G., Sutherland, R., Townend, J., Allen, M., Becroft, L., Boles, A., Boulton., C., Carpenter, B., Cooper, A.,
463   Cox, S., Daube, C., Faulkner., D., Halfpenny, A., Kato, N., Keys, S., Kirilova, M., Kometani, Y., Little, T., Mariani,
464   E., Melosh, B., Menzies, C., Morales, L., Morgan, C., Mori, C., Niemeijer, A., … and Zimmer, M.: Bedrock
465   Geology of DFDP-2B, Central Alpine Fault, New Zealand, New Zealand Journal of Geology and Geophysics.,
466   60(4), 497-518, 2017.

467   Upton P. and Craw D.: Modelling the role of graphite in development of a mineralised mid-crustal shear zone,
468   Macraes mine, New Zealand, Earth and Planetary Science Letters 266: 245-255, 2008.

469   Walder, J., and Nur, A.: Porosity reduction and crustal pore pressure development, Journal of Geophysical Research:
470   Solid Earth, 89(B13), 11539-11548, 1984.

471   Wiersberg, T. and Erzinger, J.: Origin and spatial distribution of gas at seismogenic depths of the San Andreas Fault
472   from drill-mud gas analysis: Applied Geochemistry, v. 23, no. 6, p. 1675-1690, 2008.

473   Williams, J. N., Toy, V. G., Smith, S. A. and Boulton, C.: Fracturing, fluid-rock interaction and mineralisation
474   during the seismic cycle along the Alpine Fault, Journal of Structural Geology, 103, 151-166, 2017.

475   Zhu, W., Allison, K. L., Dunham, E. M., Yang, Y.: Fault valving and pore pressure evolution in simulations of
476   earthquake sequences and aseismic slip, Nature Communications, 11, 4833, doi.org/10.1038/s41467-020-18598-z,
477   2020.
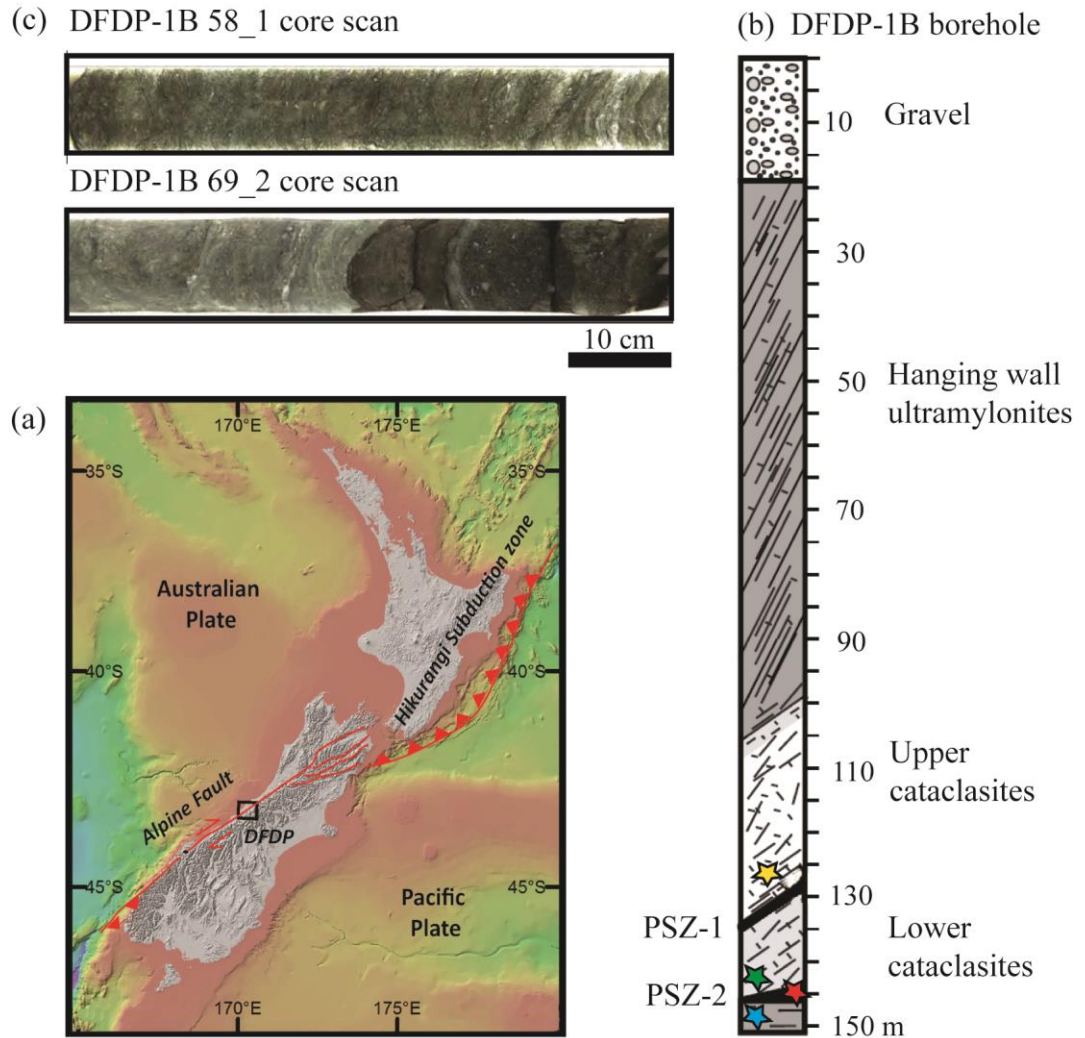
480   **Figure 1.** (a) Location map of DFDP drill sites (a bathymetric map compiled by NIWA). Drill site coordinates:
481   43°17′5″S, 170°24′22″E (b) Schematic diagram of the sampled lithologies in DFDP-1B borehole (modified after
482   Sutherland et al., 2012). (c) Scans of DFDP-1B drill core. Samples were collected from the locations indicated with
483   stars: yellow – DFDP-1B 58_1.9; green – DFDP-1B 69_2.48; red – DFDP-1B 69_2.54; blue – DFDP-1B 69_2.57.

DFDP - 1B 69-2.57

(a)
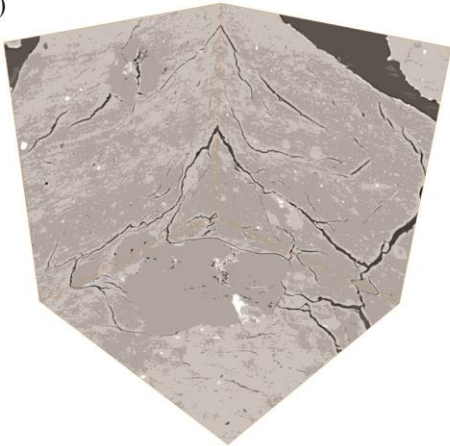
(b)
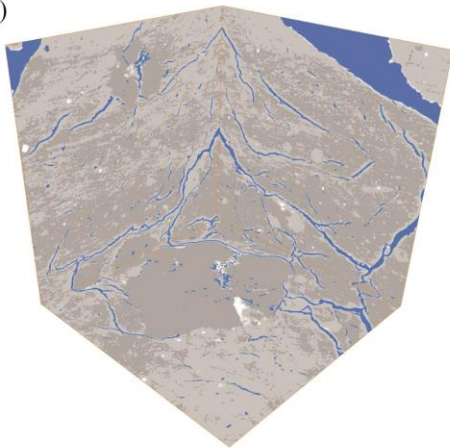
(c)
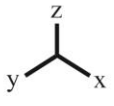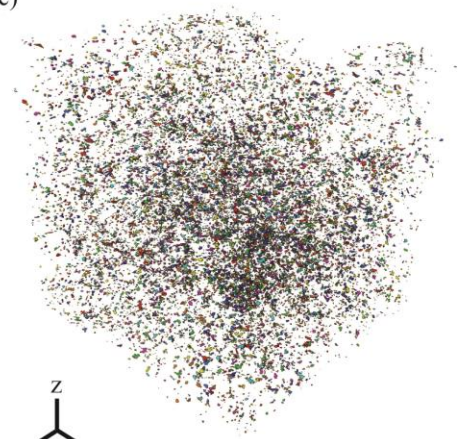
484

485 **Figure 2.** X-ray tomography data processing workflow. (a) Gray scale images in xy, xz and yz directions (b)
486 Threshold of the darkest gray scale phase in each sample, corresponding to voids (pores and fractures); (c) 3D
487 volume of the segmented pore spaces after removal of the fractures due to sample decompaction and coring
488 damaging effects.

(a) DFDP-1B 58-1.9 (upper foliated ccl)
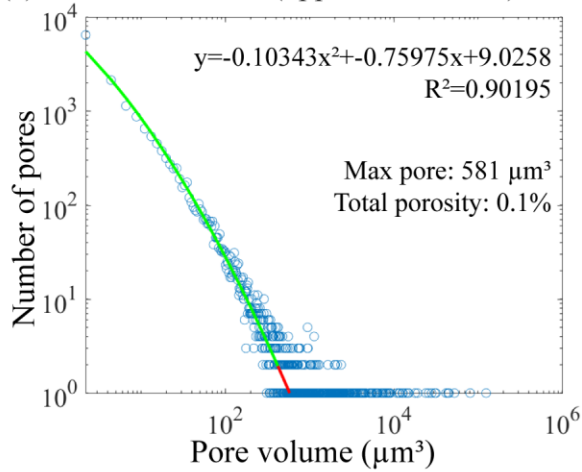
$y = -0.10343x^2 + -0.75975x + 9.0258$
$R^2 = 0.90195$

Max pore: 581 µm³
Total porosity: 0.1%

(b) DFDP-1B 69-2.48 (upper foliated ccl)

$y = -0.1545x^2 + -0.35397x + 8.8986$
$R^2 = 0.83825$

Max pore: 685 µm³
Total porosity: 0.12%

(c) DFDP-1B 69-2.54 (PSZ-2)

$y = -0.084615x^2 + -0.90712x + 10.049$
$R^2 = 0.85643$

Max pore: 862 µm³
Total porosity: 0.1%

(d) DFDP-1B 69-2.57 (lower ccl)

$y = -0.16268x^2 + -0.24165x + 8.7739$
$R^2 = 0.83608$

Max pore: 764 µm³
Total porosity: 0.24%
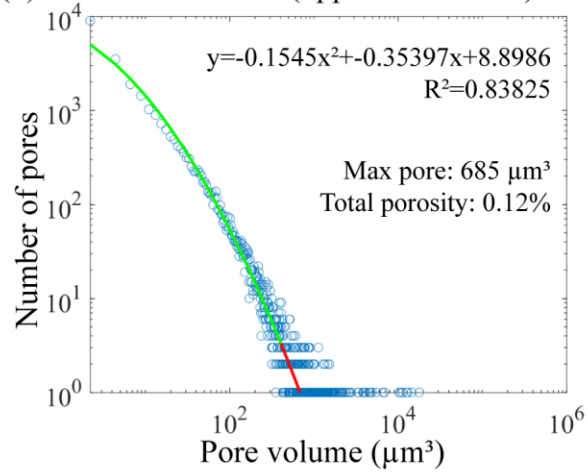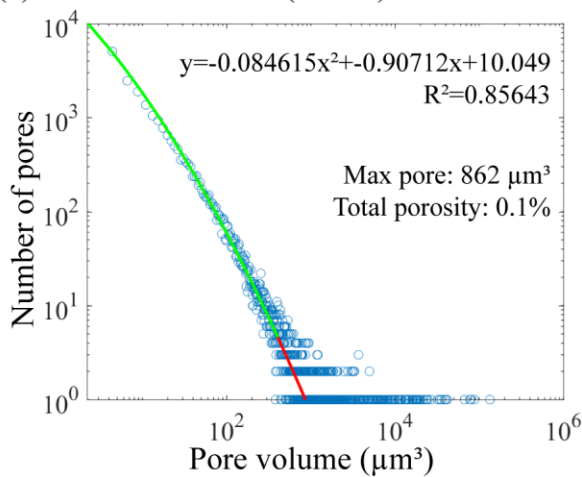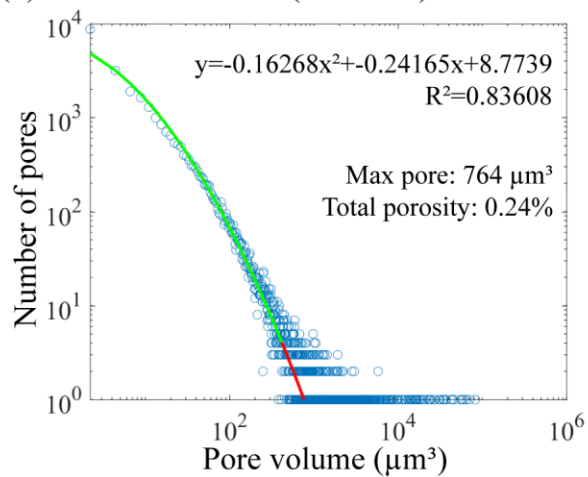
Figure 3. Plots of pore volume versus number of pores for each sample. Estimates of total porosity and size of the maximum expected pore are also shown, as well as the curve fitting function for each dataset.
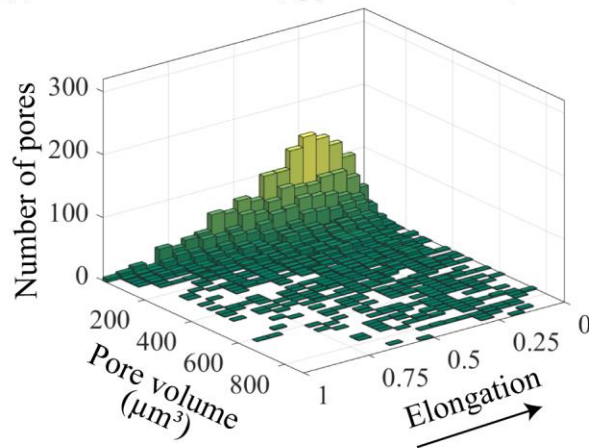
15
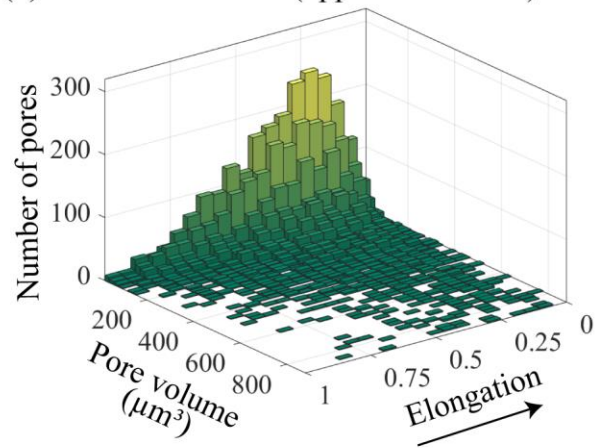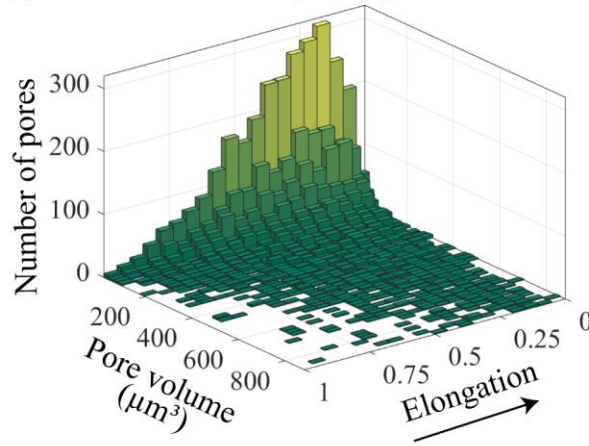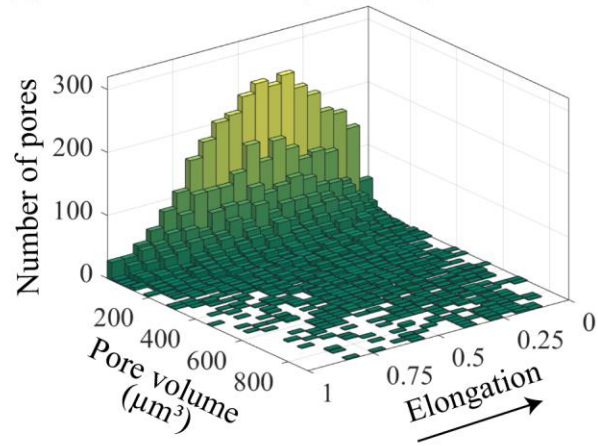
Figure 4. Bivariate histograms showing elongation versus pore volume (μm^3) and number of pores for each sample. The arrow indicates the direction of increasing elongation. Here, the elongation is defined as the ratio between the medium and the largest eigenvalues (i.e. axis) of each pore.
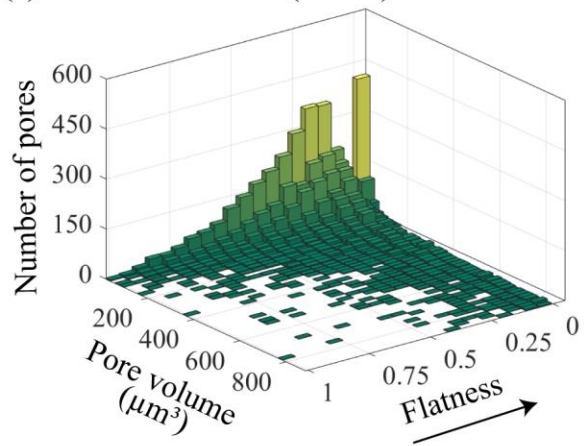
(a) DFDP-1B 58-1.9 (upper foliated ccl)
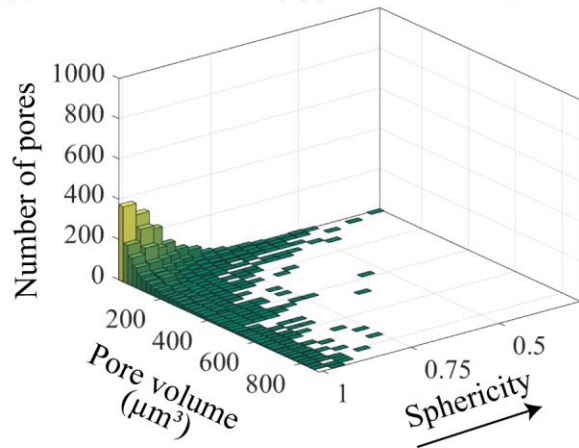
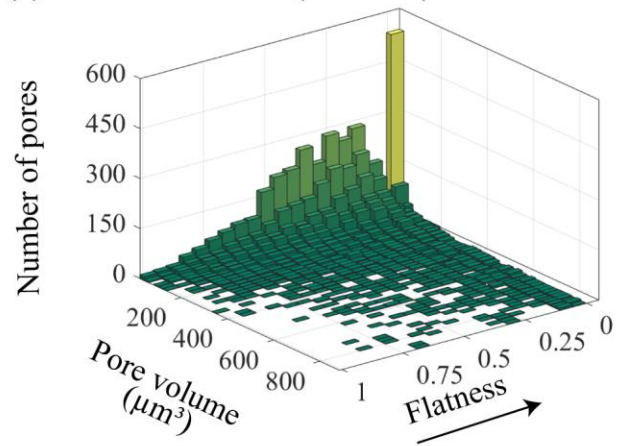(b) DFDP-1B 69-2.48 (upper foliated ccl)
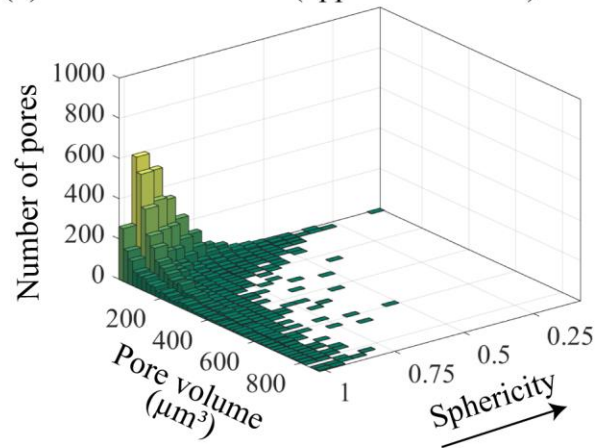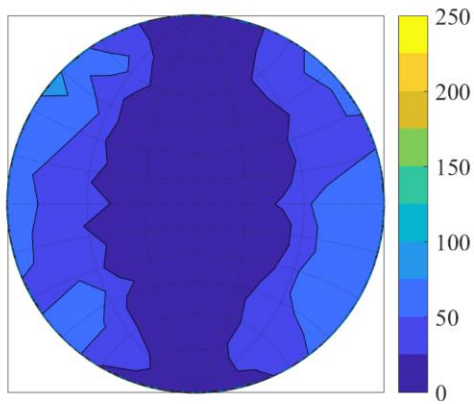
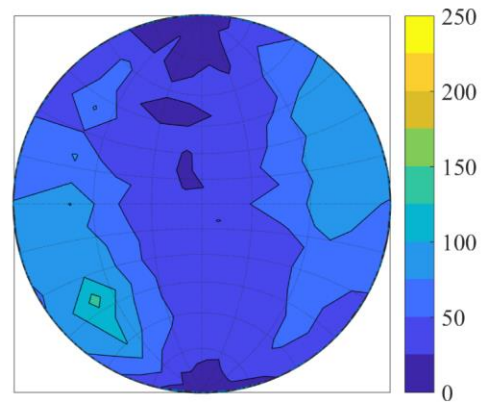(c) DFDP-1B 69-2.54 (PSZ-2)
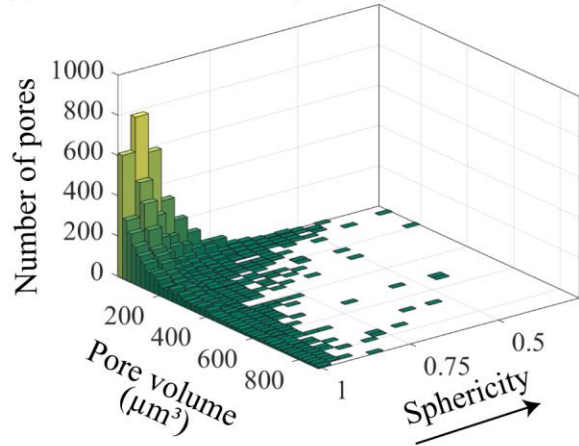
(d) DFDP-1B 69-2.57 (lower ccl)

496
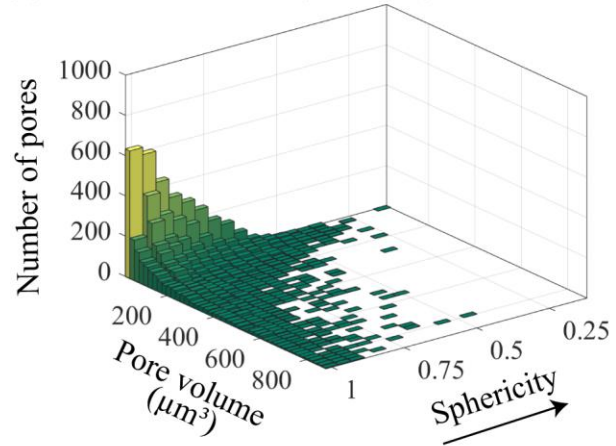
Figure 5. Bivariate histograms showing sphericity versus pore volume (μm^3) and number of pores for each sample. The arrow indicates the direction of increasing sphericity. Here, the sphericity is defined as the ratio between the smallest and the largest eigenvalues (i.e. axis) of each pore.

(a) DFDP-1B 58-1.9 (upper foliated ccl)
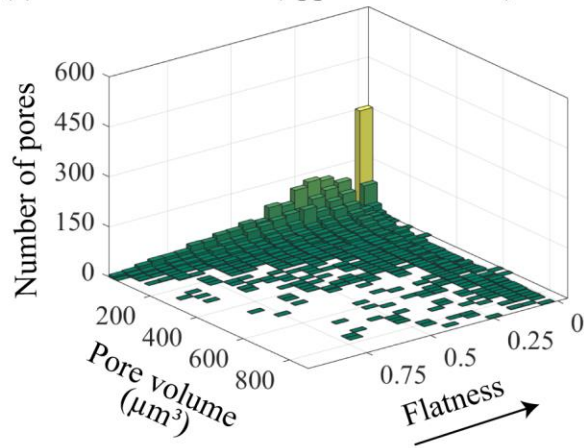
(b) DFDP-1B 69-2.48 (upper foliated ccl)
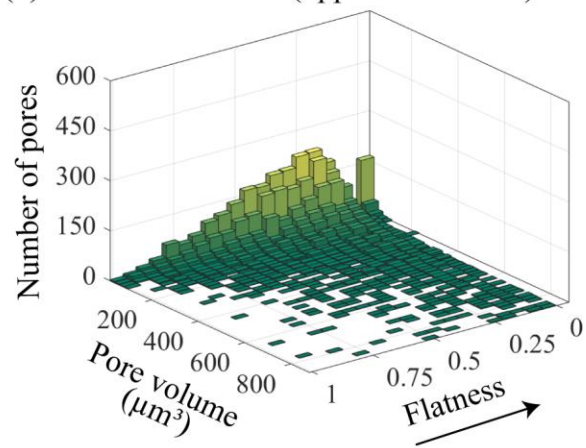
(c) DFDP-1B 69-2.54 (PSZ-2)

(d) DFDP-1B 69-2.57 (lower ccl)

500

Figure 6. Bivariate histograms showing flatness versus pore volume (µm³) and number of pores for each sample. The arrow indicates the direction of increasing flatness. Here, the flatness is defined as the ratio of the smallest and the medium eigenvalues (i.e. axis) of each pore.
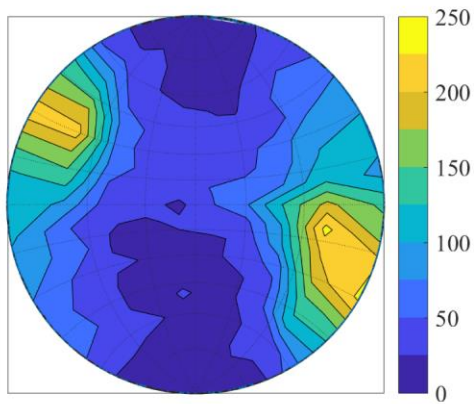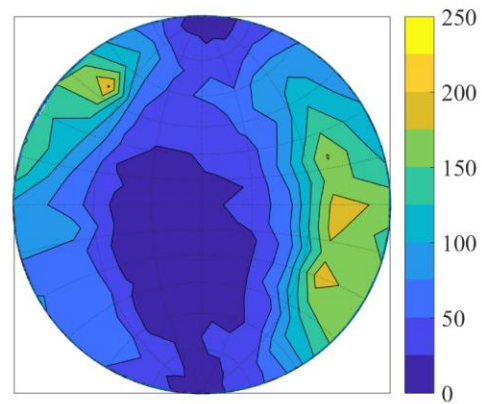
18

(a) DFDP-1B 58-1.9 (upper foliated ccl)

(b) DFDP-1B 69-2.48 (upper foliated ccl)

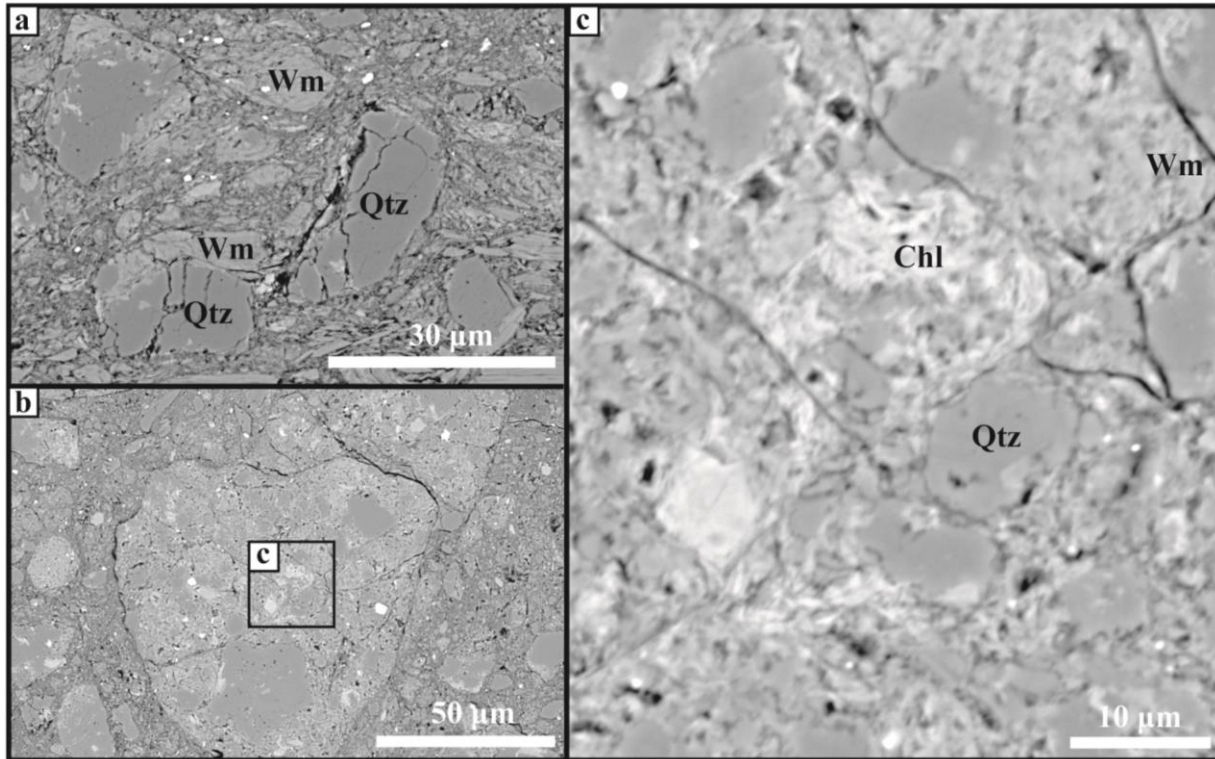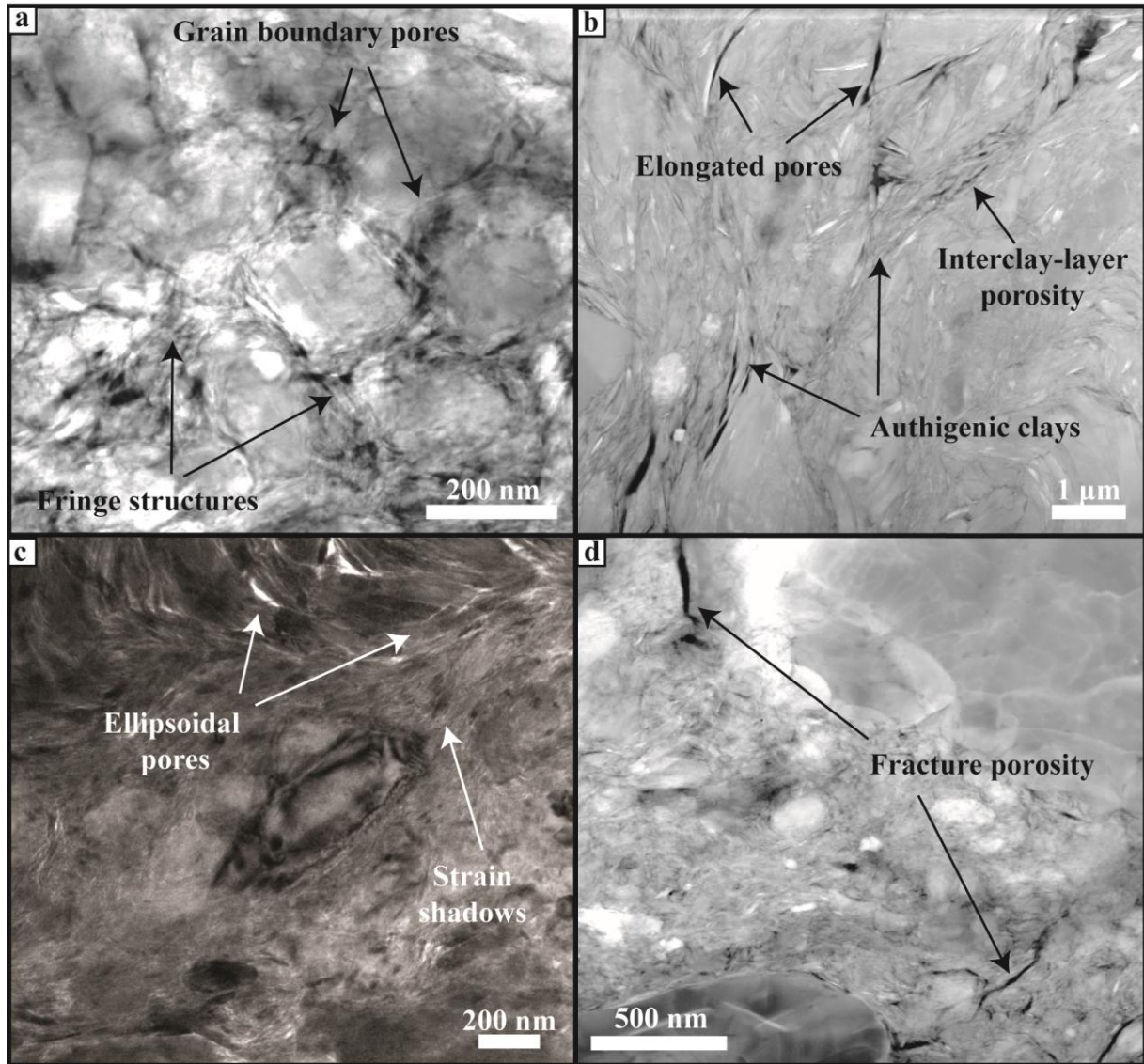(c) DFDP-1B 69-2.54 (PSZ-2)

(d) DFDP-1B 69-2.57 (lower ccl)

504

505 **Figure 7.** Distribution of pore unit orientations plotted on a lower hemisphere equal area stereographic projection
506 with a probability density contour.

507

Figure 8. Scanning electron images collected from sample DFDP 1B 69-2.48 showing the existing mineral
associations. (a) Sub-rounded and intensly fractured quartz and white mica clasts, within fine matrix material. (b)
Reworked cataclasite clasts in phyllosilicate-rich matrix. (c) Fine chlorite and white mica aggregates between quartz
clasts. (Qtz = quartz, Wm = white mica, Chl = chlorite).

Figure 9. Transmission electron microscopy images collected from the gouge sample DFDP-1B 69_2.54 (PSZ-2). (a) and (c) are bright-field (BF) images, where porosity appears as bright contrast areas. (b) and (d) are high-angle annular dark field (HAADF) images, where pores appear as dark contrasts areas. (a) TEM bright-field image of homogeneous fault gouge area. Quartz/feldspar grains, wrapped by fine authigenic clays, displaying fringe morphlogies. Pores with sub-angular shape distributed along grain boundaries. (b) HAADF image of phyllosilicate-rich gouge area. Co-existence of fine authigenic clays with coarser clay mineral grains. Elongated pores and interlayer porosity. (c) TEM bright-field image of ellipsoidal pores in phyllosilicate-rich areas. Examples of strain shadows along quartz/feldspar grains. (d) HAADF image of fracture porosity along grain boundaries of quartz/feldspar grains.